



## Geometric shape measurement and its application in bridge construction based on UAV and terrestrial laser scanner

Yitian Han<sup>a</sup>, Dongming Feng<sup>a,b</sup>, Weiwei Wu<sup>a</sup>, Xingyu Yu<sup>a</sup>, Gang Wu<sup>a,b,\*</sup>, Jixiang Liu<sup>c</sup>

<sup>a</sup> Key Laboratory of Concrete and Prestressed Concrete Structures of the Ministry of Education, Southeast University, Nanjing, China

<sup>b</sup> National and Local Joint Engineering Research Center for Intelligent Construction and Maintenance, Nanjing, China

<sup>c</sup> China Railway Construction Investment Shanxi Expressway Co., Ltd., Yuncheng, China

### ARTICLE INFO

#### Keywords:

3D reconstruction  
Point cloud  
Unmanned aerial vehicle (UAV)  
Terrestrial laser scanner  
Bridge alignment  
Optimized flight planning

### ABSTRACT

Oblique photography and laser scanning techniques are increasingly being used to measure the geometric shapes of structures. Optimizing the flight path of unmanned aerial vehicles (UAVs) in data acquisition can make the collected image data more complete with multi-view details and improve the utilization of image data in 3D reconstruction. This paper proposed a convenient UAV flight planning approach for oblique photography based on feature waypoints along with an efficient framework for automatically extracting bridge alignment from point cloud data. The application on an under-construction long multi-span girder bridge demonstrated the effectiveness of the optimized UAV flight planning method for collecting multi-view bridge images and the superiority of the rebuilt 3D model compared to commonly used flight strategies. Taking the total station data as references, the errors of the bridge alignment obtained from the point cloud collected by the frequently adopted terrestrial laser scanners (TLS) and UAV devices, respectively, achieve 4.41 mm and 10.97 mm in 142 m measured length. The analysis of the original and eliminated-slope bridge alignments illustrates the potential for using the suggested method in general large-scale bridge constructions.

### 1. Introduction

The geometric shape of bridges contains important factors for bridge inspections and assessments [1]. The geometric shape needs to be reviewed, especially in the construction stages, as the various component deformations as construction advances may have a greater detrimental effect on the structure than during the service stage [2]. Conventional devices for measuring bridge geometric shapes, including total stations and theodolites, always determine the bridge profile by collecting spatial coordinates of sparse points and generating a point-connected shape. Typically, multiple measuring stations are configured to guarantee complete coverage of the entire bridge, and high-resolution geometric shapes require dense targets, which is time-consuming and labor-intensive. Urban mapping [3], 3D modeling [4], traffic monitoring, civil engineering [5], forest monitoring [6], and other fields have recently used point clouds acquired using laser scanning and image-based approaches. In the realm of civil engineering, the 3D point cloud model has already been implemented for quality assessment of precast concrete elements [7], automated generation of FE models [8], measurement of connected precast concrete components

[9], detection of structural surface defects [10], etc.

Three-dimensional laser scanners, which can quickly obtain the 3D coordinates of the target point with laser ranging techniques, provide high automation, high resolution, and high precision [11]. Wang et al. [7] proposed an automated quality assessment technique that estimates the dimensions of precast concrete elements with geometry irregularities using terrestrial laser scanners (TLS). Ye et al. [12] proposed a method of mapping deformations and inferring movements of masonry arch bridges using point cloud data. Zhou et al. [13] proposed a series of intelligent extraction algorithms for splicing control points based on the point cloud from a TLS and adopted the strategy of local point cloud data instead of complete point cloud data to virtually pre-assemble multiple segments of the bridge. Accordingly, 3D laser scanners have the characteristics of high automation, quick measurement speed, and high measurement accuracy, which dedicates its potential to be applied to geometric shape measurements to obtain continuous bridge alignment.

In general, image-based 3D reconstruction tends to have lower accuracy compared to laser scanners [14]. Nevertheless, UAV-based oblique photography has continued to grow in popularity as a 3D reconstruction method owing to its proven advantages in capturing

\* Corresponding author at: Key Laboratory of Concrete and Prestressed Concrete Structures of the Ministry of Education, Southeast University, Nanjing, China.  
E-mail address: [g.wu@seu.edu.cn](mailto:g.wu@seu.edu.cn) (G. Wu).

photographs of hard-to-reach observation positions and providing high-resolution images at a reasonable price [15]. He et al. [16] demonstrated that consumer UAVs could reach centimeter-level reconstruction accuracy with the global bundle adjustment technique. Chen et al. [17] proposed a point cloud-based bridge inspection procedure using UAV and a series of data evaluation methods for measurement results. Xu et al. [1] suggest decomposing the full bridge three-dimensional reconstruction task into multiple distributed tasks of reconstructing bridge sub-models using sub-image sets to improve efficiency. Additionally, a series of studies have been done to improve the accuracy of image-based 3D modeling carried out by UAVs. Roberts et al. [18] proposed a method to automatically generate UAV trajectories and evaluated the method's effectiveness by 3D reconstruction of three large outdoor scenes. The results show that the trajectories planned using this method can provide 3D models with improved precision. Moon et al. [19] proposed a method for generating and merging hybrid point cloud data acquired from laser scanning and UAV-based image processing to enhance the accuracy of the UAV-based reconstruction model.

The bridge alignment, which includes information on the shape and length of the bridge as well as the angles and elevations of some components, is regarded as one of the most crucial monitoring aspects during the bridge construction process. The vertical alignment, which depicts the vertical undulation of the bridge deck, may not only reflect whether the completed bridge's elevation and plane position meet the design and specification requirements, but it can also directly show the general condition of the bridge. Delgado et al. [20] measured the deformation of a bridge using the bridge point cloud model assisted by ground control points (GCPs) and a total station. Shi et al. [21] studied the arrangement of GCP markers and route planning suitable for construction sites in measuring bridge construction alignment and investigated the influence of parameters on measurement accuracy, including flying height, angle of bundle, photo overlap, and quantity.

Previous research has shown that the majority of the commonly employed flight planning techniques for oblique photography, such as the five-way flight and tic-tac-toe flight method [22], commonly have a certain level of data redundancy, which not only consumes the acquisition time and power but also necessitates more time for modeling calculation. The planned routes using these methods typically capture images from an overhead perspective, which is well-suited for reconstructing cities and buildings as it allows for comprehensive coverage of all sides of the target object. However, when applied to bridge reconstructions, the undersides of the beams can be challenging to capture, resulting in blind areas and loss of reconstruction data in this region. Another problem is that most studies that can achieve very accurate modeling of UAV tilt photography depend on establishing GCPs [16,20,21]. However, it will probably be challenging to place targets for those massive bridges currently under construction. Moreover, manual operation is still necessary at risky places because the geographical coordinates of the GCPs need to be located by a total station in advance.

In this study, an improved UAV flight planning method for oblique photography based on feature waypoints is presented to optimize the flight path for a more effective multi-view image collection with fewer duplicate images, which is more propitious to apply to multi-span bridges. Taking bridge alignment as the studied feature, a suggested efficient bridge alignment extraction method is applied to UAV- and TLS-collected point cloud data in a field test. The extracted bridge alignments from both devices are compared to the data from the pre-installed total station measurement site. The test is conducted with no GCPs in the whole process.

The theory and the execution process of the proposed optimized flight planning for UAV oblique photography are introduced in Section 2. The working principle of laser scanners in data collection and registration is briefly described in Section 3. Section 4 outlines the efficient framework adopted in this research for bridge alignment extraction. A field test of an under-construction long multi-span girder bridge is presented in Section 5, where the results and comparisons of the methods

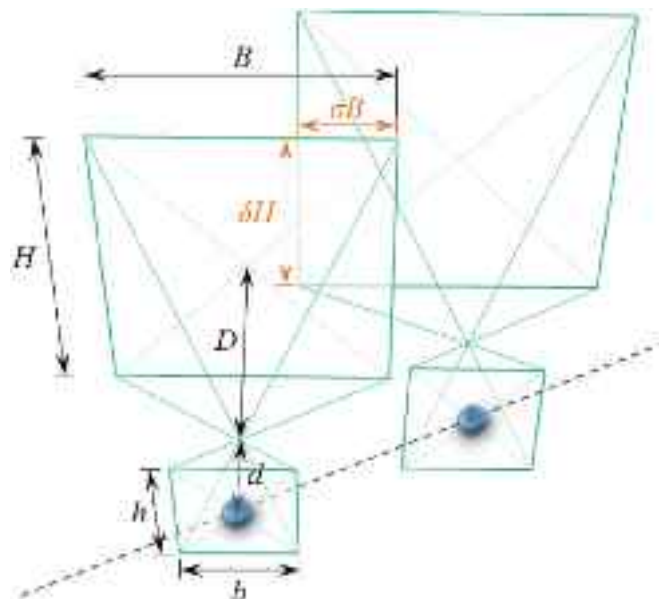


Fig. 1. Camera imaging geometry.

mentioned above are involved. Finally, the conclusions are presented in Section 6.

## 2. Optimized flight planning for UAV oblique photography

### 2.1. Calculation principle of waypoint spacing

Photogrammetry is a technique for reconstructing spatial position and three-dimensional shape using multi-view images. The feature point matching of adjacent photos is one of the crucial steps in the modeling process of oblique photography. According to the principle underlying photogrammetry and 3D reconstruction, higher information redundancy can improve the quality of the solution. To ensure the modeling quality, the neighboring photos must have an adequate overlap rate for sufficient matching feature points between every two adjacent photos. When employing UAVs as image-collection devices, the distance between adjacent waypoints on the route should be calculated strictly following the requirements for stereo images in photogrammetry. According to Ref. [23], the overlap rate should be at least 60% without setting up ground control points.

Fig. 1 depicts the geometric relationship of UAV camera imaging, where the camera sensor size is  $b \times h$  mm, the focal length is  $d$  mm, the object distance is  $D$  mm, the shooting range of the screen is  $B \times H$  mm, and the horizontal overlap rate is  $\sigma$ . The horizontal waypoint spacing  $S_{xy}$  can be obtained by

$$S_{xy} = (1 - \sigma)B = (1 - \sigma)\frac{Db}{d} \quad (1)$$

Assuming the vertical overlap rate is  $\delta$ , the vertical waypoint spacing  $S_z$  can be obtained by

$$S_z = (1 - \delta)H = (1 - \delta)\frac{Dh}{d} \quad (2)$$

### 2.2. Optimized flight planning for UAV oblique photography

The optimized flight path in this study is generated by setting feature waypoints on the existing rough 3D model. Feature waypoints refer to the control points of the flight path that are created based on structural geometric characteristics and are typically placed at the geometry corners of some components. The calculation method for interpolation waypoints using feature waypoints is described in this section, and the

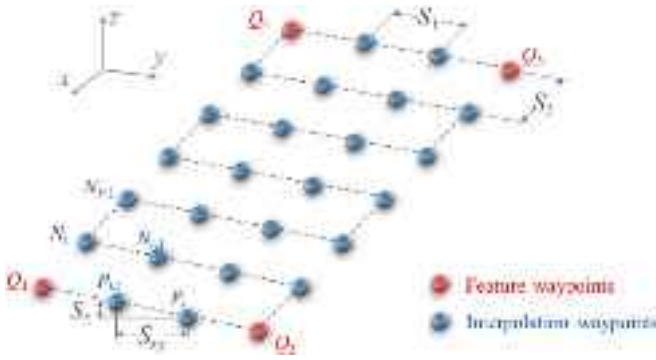


**Fig. 2.** Oblique photography flight path planning based on feature waypoints

detailed execution process, including the selection of feature waypoints, will be introduced in [Section 2.3](#). By establishing specific feature waypoints, feature lines are created by connecting in succession, and interpolation waypoints are generated in the measurement region of a straight line, a polyline, or a curve. For instance,  $Q_1$ ,  $Q_2$ ,  $Q_3$ , and  $Q_4$  in [Fig. 2](#) are the feature waypoints, and the line connecting  $Q_1$  and  $Q_2$  is a feature line. When interpolation waypoints are inserted on the line  $\overrightarrow{Q_{k-1}Q_k}$ , the ratio of the horizontal waypoint spacing  $S_{xy}$  and the vertical waypoint spacing  $S_z$  equals the ratio of the horizontal distance  $L_{xy}$  and vertical distance  $L_z$  between  $Q_{k-1}$  and  $Q_k$ , and can be calculated by

$$s = \frac{S_{xy}}{S_z} = \frac{L_{xy}}{L_z} = \frac{\sqrt{(x_k - x_{k-1})^2 + (y_k - y_{k-1})^2}}{|z_k - z_{k-1}|} \quad (3)$$

The interpolation waypoint spacing for the same feature line may differ when determined using the horizontal or vertical minimum overlap rate. Denser interpolation waypoints should be employed to guarantee that the overlap rate in both directions satisfies the specifications. Assuming the horizontal and vertical overlap rate is at least  $\sigma$  and  $\delta$ , the horizontal and vertical waypoint spacing calculated by  $\sigma$  and  $\delta$  is  $S_{xy}$ ,  $\sigma$  and  $S_z$ ,  $\delta$ , when  $\frac{(1-\sigma)b}{(1-\delta)h} \leq s$ , i.e.  $S_{xy}, \sigma/S_z, \delta \leq s$ , the spacing between adjacent waypoints should be calculated according to the horizontal overlap rate  $\sigma$  as

$$\begin{cases} S_{xy} = S_{xy,\sigma} = (1 - \sigma)B = (1 - \sigma)\frac{Db}{d} \\ S_z = S_{xy}/s \end{cases} \quad (4)$$

Otherwise, it should be calculated according to the vertical overlap rate  $\delta$  as

$$\begin{cases} S_z = S_{z,\delta} = (1 - \delta)H = (1 - \delta)\frac{Dh}{d} \\ S_{xy} = s \cdot S_z \end{cases} \quad (5)$$

Let  $P_i$  be a waypoint between  $Q_{k-1}$  and  $Q_k$ , and  $P_1 = Q_{k-1}$ , the

position of  $P_i$  ( $i \geq 2$ ) can be calculated by

$$P_i = P_{i-1} + \frac{\sqrt{S_{xy}^2 + S_z^2}}{\| \overrightarrow{Q_{k-1}Q_k} \|} \overrightarrow{Q_{k-1}Q_k}, i \geq 2 \quad (6)$$

It should be noted that, sometimes, for convenience, an equally minimum overlap rate is set both horizontally and vertically, and then the judgment condition  $S_{xy}, \sigma/S_z, \delta \leq s$  will be simplified to  $b/h \leq s$ .

This concept can be extended to the feature area. A feature area in the region bounded by the adjacent feature waypoints like  $Q_1$ ,  $Q_2$ ,  $Q_3$ , and  $Q_4$  in [Fig. 2](#). Assuming the forward overlap rate is  $\xi$ , and the side overlap rate is  $\eta$ , the forward spacing  $S_1$  and the side spacing  $S_2$  between adjacent waypoints are calculated by

$$S_1 = (1 - \xi)B = (1 - \xi)\frac{Db}{d} \quad (7)$$

$$S_2 = (1 - \eta)H = (1 - \eta)\frac{Dh}{d} \quad (8)$$

Numbering the feature waypoint  $Q_1$  as waypoint  $N_1$ , the coordinates of  $N_i$  on the same heading are:

$$N_i = N_{i-1} \pm \frac{S_1}{\| \overrightarrow{Q_1Q_2} \|} \overrightarrow{Q_1Q_2} \quad (9)$$

The coordinates of the first waypoint  $N_{i+1}$  on the next adjacent route are calculated by

$$N_{i+1} = N_i + \frac{S_2}{\| \overrightarrow{Q_2Q_3} \|} \overrightarrow{Q_2Q_3} \quad (10)$$

### 2.3. Execution process

Generally, for different structural components, the feature points can be manually selected at appropriate positions on the rough model according to the geometric features of the components to establish the feature lines or feature areas. The principle of determining feature waypoints is to have the given route cover as much area as feasible with consistent parameters, particularly the gimbal camera's angle. Geographic position data is included in the feature waypoints since it is present in the preliminary 3D bridge model. According to this data and the relative position relationship between the flight path and the feature line, the UAV's custom and refined flight path can be planned.

After sparsely marking the feature waypoints which cover every target part of the bridge, their position coordinates in the rough 3D model are read. The final flight routes are then created in two steps, including a) automatically determining interpolation waypoints based on feature lines and feature areas and b) extending to generate UAV oblique photographic routes. The final flight point should be shifted  $D$  mm outward to account for the shooting distance between the UAV and the observed plane. The target pixel accuracy, which is the ratio of the

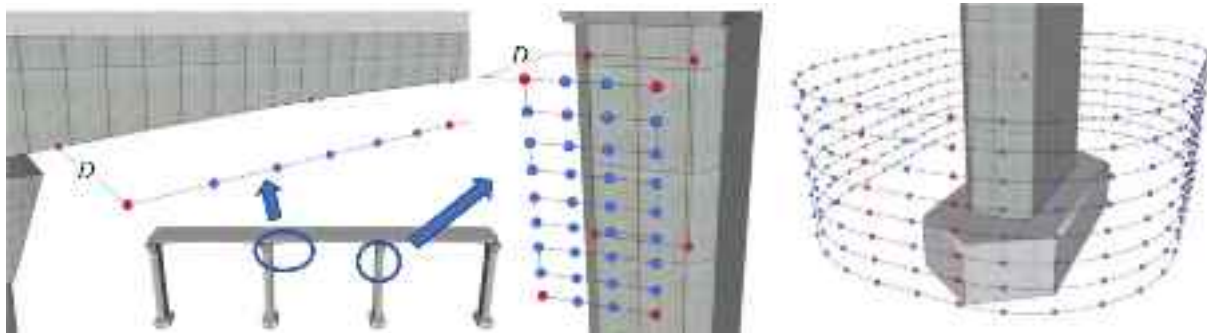


**Fig. 3.** Schematic diagram of several typical optimized flight paths.

field of vision (FOV) to the resolution and indicates the physical distance a pixel represents in the real world, is always what determines this distance, referring to the camera imaging geometry in Fig. 1. The blue waypoints in Fig. 3 represent the final interpolation points. By configuring the pitch angle of the gimble camera and flight speed, these parameters are compiled into a .kml file along with the geographic position information of each waypoint and then imported into the UAV so that it can read the file and execute the flight task accordingly.

The route planning suggestions for different parts of the bridge are as follows:

- For beams, the feature line or feature area is suggested to be established along the longitudinal dimension as it is obviously longer than the other dimensions. Flight routes of the different bridge's sides are typically planned separately due to their varied orientations, and the feature points are naturally selected at the four corners of each rectangular surface. A part of the flight routes should be selected to take images with oblique angles to ensure overlap at their interfaces so that images from different sides can be successfully stitched.
- For piers, similar to how it works with beams, distinct routes can be generated for each surface, or circular routes can be applied. When adopting the circular route, four corners of the rectangular section of the pier can be selected to generate four feature lines from the intersection line between the pier and the ground in the rough model. Following estimating the outward moving distance  $D$ , the adjacent feature lines are connected by arcs to form a ring. The entire route is generated by replicating the ring upward with an interval determined by the side overlap rate and connecting them consecutively.
- For cables, feature waypoints are typically marked at both ends of each cable to generate feature lines which could also be broken lines linking numerous feature waypoints along a curved cable. Each cable should involve a minimum of two routes if neighboring routes supplement the side view photographs, or three routes if nearby routes are unavailable.

### 3. Laser-based point cloud data collection

3D laser scanning technology is frequently adopted in various measurement tasks. The laser rangefinder actively emits laser light and simultaneously receives the signal reflected from the surface of the natural object so that the distance can be measured. 3D laser scanners can realize a fast and accurate 3D model construction for various large-scale irregular, complex buildings and environments with insufficient light, which provides an important technical guarantee for complex construction engineering design.

The process of collecting point cloud data using a terrestrial laser scanner (TLS) typically involves: 1) a scanning range pre-test, 2) the planning of survey sites, 3) the collection of point cloud data site by site, and 4) the registration of point cloud data. In order to determine an appropriate measurement site plan, the pre-test in the first step is necessary to be conducted to evaluate the measurement range of the TLS device in the current environment. Since the data collected by each TLS station is relative to its position, it is necessary to register the point data from all scanning stations into one uniform coordinate system by estimating their consistency. There are typically three ways of point cloud data registration: automatic registration with targets (ball target and panel target), automatic registration without targets, and manual registration. The target should be used when the structure surfaces are uniformly symmetrical and smooth because the point cloud could be difficult to match automatically or cause mismatches. The success and accuracy of registration are significantly affected by the overlap rate and the objects with recognizable geometric features in the overlap region. Therefore, to ensure the success of point cloud registration, the measuring units of the two stations need a sufficient overlap. Besides, it is suggested to have objects with geometric properties distinct from the

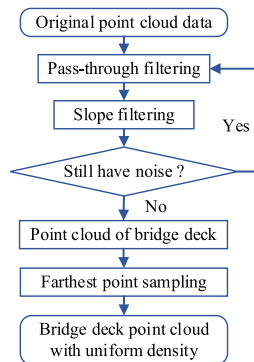


Fig. 4. Flowchart of point cloud data preprocessing.

surrounding area they both cover if no artificial targets are used.

## 4. Bridge alignment extraction based on point cloud data

### 4.1. Data preprocessing

In order to ensure the efficiency and accuracy of the bridge alignment extraction, denoising filtering, and downsampling algorithms are used to remove the noise data of the bridge deck accessories and piled sundries to obtain the point cloud data of the bridge deck. The preprocessing process of point cloud data is shown in Fig. 4.

Since the bridge deck point cloud has a wide distribution range along the bridge direction and a limited distribution range in the transverse bridge direction and height direction, this paper first uses a pass-through filter to remove invalid points and outliers quickly. The point cloud set  $P$  can be filtered by

$$\begin{cases} x_{\min} - \Delta_x \leq x_i \leq x_{\max} - \Delta_x \\ y_{\min} - \Delta_y \leq y_i \leq y_{\max} - \Delta_y \\ z_{\min} - \Delta_z \leq z_i \leq z_{\max} - \Delta_z \end{cases} \quad (11)$$

where  $(x_i, y_i, z_i)$  is the coordinate of the point  $p_i$  in the set  $P$ ; the subscript  $\min$  and  $\max$  denote the minimum and maximum values of all point coordinates on the corresponding axis, respectively.

Considering most of the bridge deck slopes are generally gentle, the point cloud filtering algorithm based on the slope is then used to segment the point cloud data of the bridge deck according to the slope filtering algorithm. The steps can be summarized as follows: a) divide the point cloud into grids, b) determine the seed point and c) reserve the required points based on the threshold. Even when the data currently satisfies the threshold requirements, there may still be noise remaining. However, this noise can be easily eliminated by pass-through filtering once more, accounting for the gap between the noise and the actual point cloud of the bridge deck.

For terrestrial laser scanners (TLS), there is a blind area slightly below the scanning head, and the obtained data is dense in the close and sparse in the distant. The measurement stations are arranged along the bridge, so the place between two adjacent stations will be captured by both adjacent stations, and the point in the middle of the bridge will be denser. The point cloud density at either end of the span is sparse compared to the middle of the bridge since there is only one station's data. The farthest point sampling (FPS) algorithm is used to downsample the bridge deck data to reduce the computation of subsequent bridge alignment extraction as well as eliminate the influence of point density. The strategy is first to take a point from the origin set and put it into the empty target point set, then iteratively renew it by constantly taking the farthest point from the origin set to the target point set. The pseudocode of the FPS algorithm is as follows:

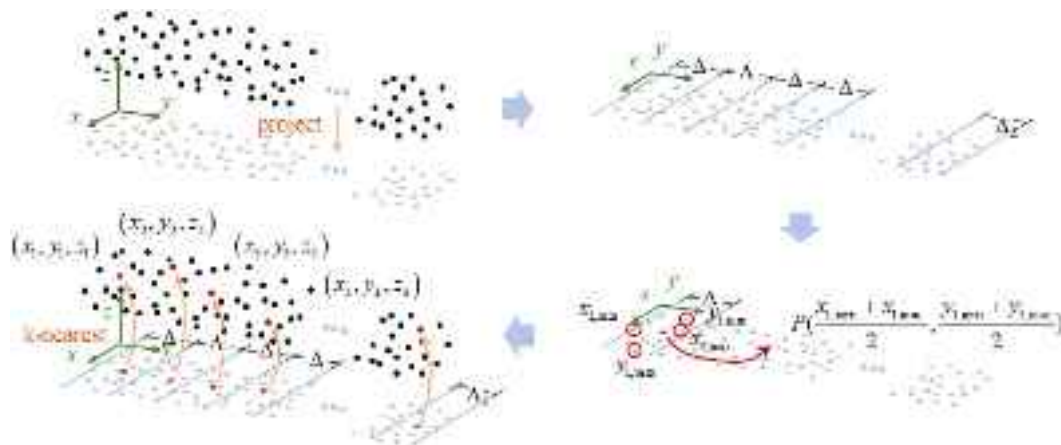


**Fig. 5.** Implementation process of the fixed-step search method.

---

**INPUT:**  $point$  = Pointcloud Data;  $npoint$  = Target Sampling Number

**RETURN:**  $point\_s$  = sampled point cloud

Calculate the barycentric coordinate of  $point$  as the initial point

Calculate the distance from each point to the barycentric coordinates

Record the index value of the point with the largest distance in  $point$  and take it from  $point$  to  $point\_s$

**repeat**

**for**  $i$  in  $\text{length}(point\_s)$

        A. Calculate the minimum distance from each point  $i$  in  $point$  to each point  $t$  in  $point\_s$ :

$$\text{MinDist} = \left\{ \min\{d_{11}, d_{12}, \dots, d_{1L}, d_{i1}\}, \min\{d_{21}, d_{22}, \dots, d_{2L}, d_{i2}\}, \dots, \min\{d_{i1}, d_{i2}, \dots, d_{iL}, d_{it}\} \right\}$$

        B. Find the index of the maximum value in this set of distances:  $r = \text{index}(\max\{\text{MinDist}\})$

        C. Take  $point(r)$  from  $point$  to  $point\_s$

**until**  $\text{length}(point\_s) = npoint$

---

#### 4.2. Bridge alignment extraction

This paper adopted two bridge alignment extraction methods: the fixed-step search method and the centroid of slice method. The results and comparison of these two methods in extracting bridge alignment are presented in Section 5.3.

##### 4.2.1. Fixed-step search method

The fixed-step search method is first taken into consideration in this work to quickly extract bridge alignment from numerous point cloud data due to its straightforward theory and minimal computation. The implementation process is shown in Fig. 5. Assume that the axis along the bridge's longitudinal direction is  $x$ , along the bridge's transverse direction is  $y$ , and the vertical direction is  $z$ . Project the three-

dimensional point cloud data to the  $xy$  plane, then projected points are divided by a fixed-step  $\Delta$ . Find  $x_{i, \min}$ ,  $x_{i, \max}$ ,  $y_{i, \min}$  and  $y_{i, \max}$  of step  $i$ , and obtain  $P\left(\frac{x_{i, \min} + x_{i, \max}}{2}, \frac{y_{i, \min} + y_{i, \max}}{2}\right)$ . Using the k-nearest algorithm, the nearest point  $P$  in the original three-dimensional point cloud is found as the key point of this step. Apply the above procedure to all the steps to extract all key points. To be noticed, the length of the last step  $\Delta_L$  may be less than  $\Delta$ , then the  $\Delta$  in the last step length should be replaced by  $\Delta_L$ .

##### 4.2.2. Centroid of slice method

This paper also adopted a centroid of slice method to obtain the bridge alignment data, which uses the centroid of the point cloud near the chosen slices to represent the key point of the bridge alignment. As shown in Fig. 6, taking the minimum coordinate point in the longitudinal direction of the bridge as the starting point, select an appropriate

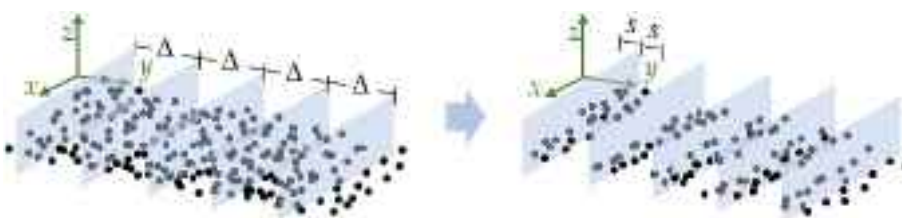


**Fig. 6.** Point cloud blocks extraction along the longitudinal direction of the bridge.

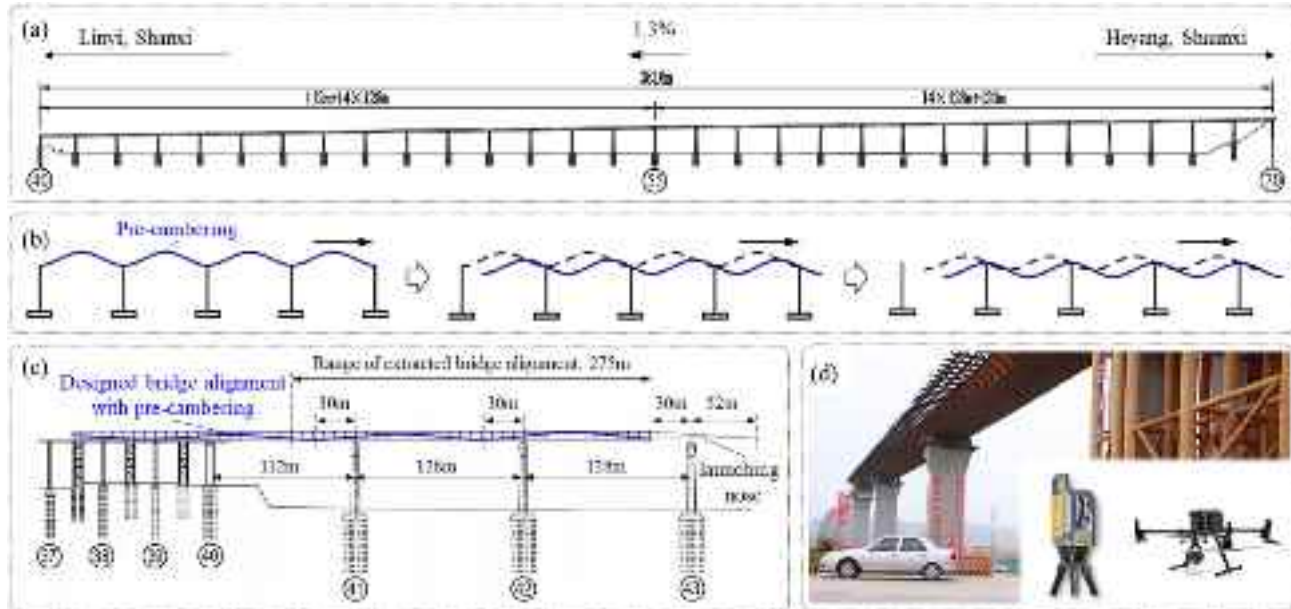


**Fig. 7.** Linyi Yellow River Bridge: (a) spans layout of the entire bridge, (b) incremental launching process schematic of the continuous steel girder, (c) current construction progress, and (d) construction site and devices. (For interpretation of the references to colour in this figure legend, the reader is referred to the web version of this article.)

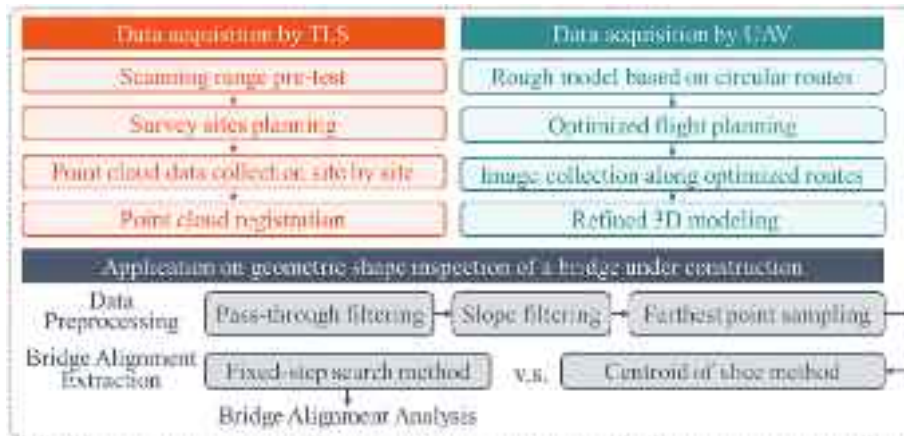


**Fig. 8.** Flowchart of the field test.

interval  $\Delta$  to generate a series of slices along the bridge's longitudinal direction. Then select the point cloud within the same distance  $s$  from the front and rear sides to form a point cloud block. The key point  $(x_i, y_i, z_i)$  of the block  $i$  can be obtained by calculating the centroid of the point

cloud of it as  $\left(\frac{1}{n} \sum_{j=1}^n x_i, \frac{1}{n} \sum_{j=1}^n y_i, \frac{1}{n} \sum_{j=1}^n z_i\right)$ . The bridge alignment

shape is created by connecting the key points in the last step.  $\Delta$  is selected according to the required sampling interval. If the slope and density of the point cloud are uniform, the value of  $s$  will not significantly affect the outcome. If the slope is not, it is advisable to decrease the value of  $s$  while ensuring adequate data points to be averaged within the interval of  $2s$ . It should be noted that the value of  $s$  is not limited by  $\Delta$ . Sometimes high-density sample points are required, in which case the slice spacing is small and  $s$  may be larger than  $\Delta/2$ , causing the averaged sections to overlap.

## 5. Field test

### 5.1. Test information

The Linyi Yellow River Bridge is an extra-large expressway bridge under construction across the Yellow River in China. The main bridge has a total length of 3816 m and is divided into two joints of  $(112 + 14 \times 128) + (14 \times 128 + 120)$  m, as indicated in Fig. 7(a). There is no flat bend in the main bridge plane, and the longitudinal gradient is 1.3%. The upper structure adopts steel box composite beams with a height of 6.28 m at the center line of the beams, which are launched from both ends for construction. The heights of all the main bridge piers, rectangular with variable-section hollow thin walls, range from 53 to 99 m.

To reduce the deflection under load, the pre-cambering design of the bridge is carried out to reserve the correction amount in the opposite direction of the deflection. The pre-cambering alignment of each span should be approximate to a quadratic parabola. The steel girder is subjected to the "rising together and falling together" principle throughout the incremental launching construction process, as illustrated in Fig. 7



**Fig. 9.** Rough model obtained from circular route acquisition: (a) top view and (b) bottom view.



**Fig. 10.** Flight planning of the test bridge: (a) pier route, (b) bridge side route, (c) deck top route, and (d) girder bottom route.

(b). The launching nose was 52 m beyond pier 43# when this test was conducted, such as in Fig. 7(c).

DJI M300 RTK and Trimble X7 were employed in this test as UAV and TLS acquisition equipment, respectively, to simultaneously collect the point cloud data of the bridge from piers 40# to the heading end of the launching nose. The flowchart of this test is outlined in Fig. 8.

The Trimble X7 has an 80 m ranging capability, a 2 mm ranging accuracy, and 21" of angular accuracy, which can collect more than 500,000 points every second. Additionally, it is merely 178 mm × 353 mm × 170 mm in size. Accordingly, the instrument is portable for on-site measurement with high accuracy, making it suitable for the majority of engineering application scenarios. From the scanning range pre-test, the effective scanning range of this device is a radius of 40 m that is centered on its site. The density of points in the scanned overlapping areas between each site is evaluated to facilitate subsequent point registration when setting out sites. To ensure the accuracy of the collected point cloud data and sufficient overlap rate for registration, a total of 18 sites were set up for TLS data acquisition in this research.

DJI M300 RTK uses a real-time kinematic (RTK) technique, whose positioning accuracy can achieve 1 cm horizontal and 1.5 cm vertical. The UAV equips the camera model Zenmuse H20T which has focus lengths from 1 m(wide)/5 m(zoom) to  $\infty$  and has a resolution of 5184 ×

3888(zoom)/4056 × 3040(wide). The detailed process of UAV reconstruction using optimized flight planning will be introduced in Section 5.2.1.

## 5.2. 3D reconstruction

### 5.2.1. 3D reconstruction based on the UAV method

The high-efficiency circular oblique photography route was used to acquire bridge images and build the rough three-dimensional model of the Linyi Yellow River Bridge, which is used to transmit the position information between the optimized-flight UAV and the bridge. The overlap rate is set to 70%.

The bridge top and bottom views of the rough model are shown in Fig. 9. Circular routes always have a wide modeling range and fast modeling speed, and the bridge model can be quickly established with a small amount of data with high efficiency. Due to the long shooting distance and blind areas of the camera, such as the bridge bottom, the model is badly crude, especially in some details. The bottom texture of the bridge deck in the 3D model is missing, and the reconstruction of the flanks of the steel bridge deck is incomplete.

The flight trajectory of the UAV is composed of a series of high-precision point coordinates based on GNSS. The flying precision of the

**Table 1**

Comparison of multi-group data combinations.

	Top view	Bottom view	Pier
F			
F + GB			
F + BS + GB			
P + BS + DT + GB			

\* F = five-way flight, P = pier route, BS = bridge side route, DT = deck top route, GB = girder bottom route.

waypoint can achieve centimeter-level when combined with RTK technology. Based on the geographic location information and the rough 3D model of the bridge, the UAV flight path close to the bridge is planned to gather multi-view photos according to the target collection area and the required accuracy.

This experiment carried out the following routes:

- Pier route (P): circumferential flight routes for each pier from 41# to 43# (Fig. 10(a));
- Bridge side route (BS): the routes below the bridge deck are inclined upward to photograph the bottom of the bridge, and those above the bridge deck are inclined downward to the deck (Fig. 10(b));
- Deck top route (DT): the UAV camera captures photos directly facing the bridge deck from about 10 m above the top of pier 40# to the end of the launching nose (Fig. 10(c));

d. Girder bottom route (GB): underneath the bottom of the two-and-a-half pushing-out spans and the launching nose (Fig. 10(d)).

The five-way flight is also conducted in this test, serving as a comparison. The results of modeling with various data combinations are shown in Table 1. It should be noted that all the data in this field test is collected without setting any ground control points (GCPs). The overlap rates are forward 80% and side 70% for the five-way flight, and 70% for the proposed strategy. The multi-view image comparison in Table 1 reveals how different models perform when data from different routes are incorporated. Due to the visual blind area under the bridge in five-way flight, the model built on the five-way flight data missed all the details beneath the girder, notably of the support area, whereas the top view of it is much clearer. The last model of Table 1, which is entirely built on the images collected through the optimized routes, exhibits a



Fig. 11. Point clouds of the deck acquired by UAV.

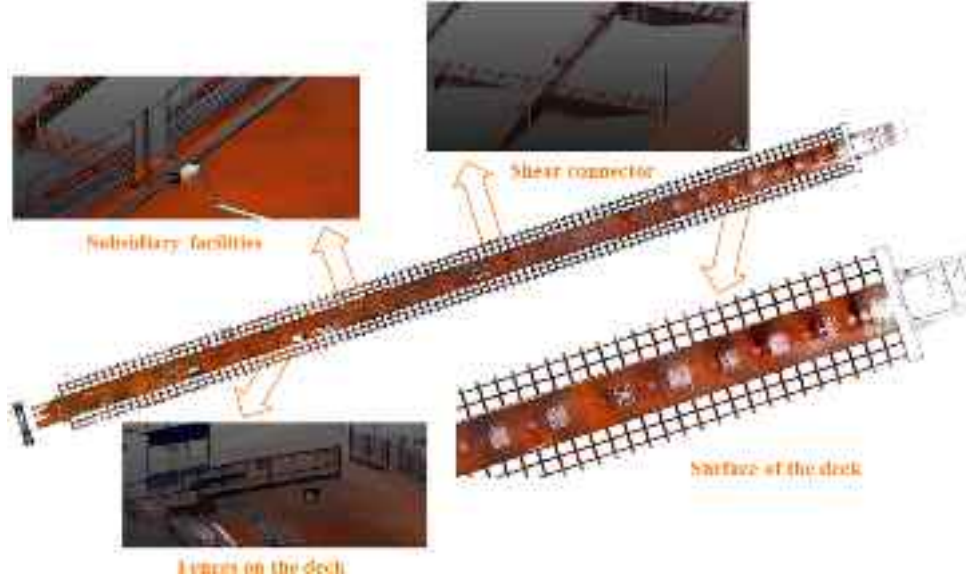


**Fig. 12.** Point clouds of the deck acquired by TLS.

**Table 2**  
Point clouds of the deck acquired by TLS.

	UAV	TLS
Filtered		
Resampled		

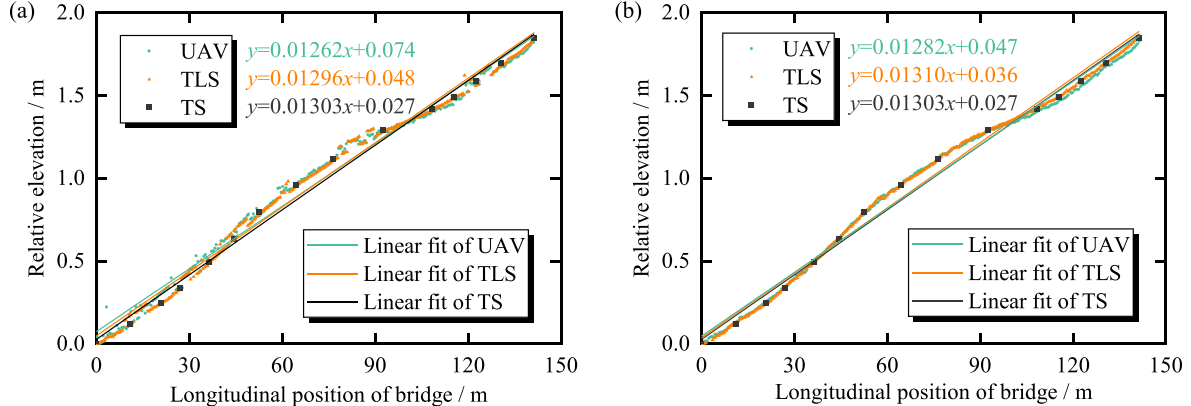


**Fig. 13.** Comparison of the measurement data: (a) fixed-step search method, and (b) centroid of slice method.

higher level of refinement and integrity.

To enhance the girder-bottom view of five-way flight data, the second model of Table 1 includes girder-bottom routes' data in five-way flight data. The girder's bottom textures, however, have still not been reconstructed. This is most likely caused by the fact that there is little overlap between these two sets of data, which results in a shortage of feature points that can be matched. Therefore, the third model was further expanded with bridge-side routes' data. Unlike the second model, the third model shows the texture of the girder's bottom but is still not as delicate as the last, particularly at some thin components like bracings. The reason is that all the images collected from the optimized routes are captured continuously along the bridge with similar pixel accuracy and overlap rates. Accordingly, consistent configures are recommended when incorporating data from various routes to achieve better performance.

The point cloud of the top surface of the deck acquired by the UAV is separated, as seen in Fig. 11, for the following bridge alignment extraction.

#### 5.2.2. 3D reconstruction based on the TLS method

Fig. 12 displays the final complete bridge deck point clouds and some details after registering each station's point clouds. The three-dimensional geometric shape of the bridge has been meticulously reconstructed, regardless of the deck's top surface or the subsidiary facilities.

Due to the high pier constraint and the device's restricted measurement range, the laser scanner only collected point cloud data for the bridge deck. For the sake of fairness, only a subset of the UAV routes that gather the bridge deck data are included in the time comparison between the two devices. These routes consist of the deck top route (DT)

**Table 3**

RMSE of the extracted bridge alignment (mm).

Method	UAV	TLS
Fixed step search method	19.72	11.13
Centroid of slice method	10.97	4.41

and a portion of the bridge side route (BS) located above the deck. Compared to TLS, which took about 1.8 h to acquire data and 2.5 h to manual registration for a 275 m range of the bridge deck, employing UAV cost approximately the same time in total, with 2.75 h (rough model: 1 h, flight planning: 0.25 h, image acquisition along the optimized routes: 1.5 h) collecting multi-view photos and 2 h building the 3D model. Moreover, both two devices can be done by just one operator, making them ideal for engineering measurement.

### 5.3. Result of bridge alignment extraction

#### 5.3.1. Preprocessed point cloud

The point cloud data was first processed according to the procedure introduced in Section 4.1. Point clouds on the bridge deck were separated based on pass-through filtering, and subsidiary facilities protruding from the deck surface were removed based on slope filtering. Then the farthest point sampling algorithm is used to downsample and remove the influence of the uneven density of the point cloud. The processing results are shown in Table 2.

#### 5.3.2. Extracted bridge alignment

The fixed-step search and centroid of slice methods are used to process the bridge deck data and extract the bridge alignment at the target position. The point cloud data within this 142 m are analyzed using the total station data as a reference. The  $\Delta$  of both the fixed-step search method and the centroid of slice method is set to 0.5 m, and the  $s$  of the centroid of slice method is set to 0.3 m. The point results are shown in Fig. 13, and their root mean square errors (RMSE) are listed in Table 3. As can be seen, the centroid of slice method shows higher accuracy in applying the bridge alignment extraction. The reason is that the centroid of slice method considers the distribution of all points around the slices, giving it a greater tolerance for those limited unexpected point cloud data. The fixed-step search method, determining one point from each step range as its representative point for the bridge alignment, is easily influenced by other items on the deck or component assembling deviation. Compared with the UAV tilt photography model, the 3D information obtained by the laser scanner has higher accuracy. With respect to the measured length of 142 m, the RMSE of the centroid of slice method utilizing TLS is 4.41 mm (0.031%) which is practical for the measurement requirements of bridge application scenarios. By linear fitting the points extracted from the three devices, it can be seen that the

slope is consistent with the design value of the longitudinal slope of 1.3%. Again, the result of the laser scanner is closer to the reference than that of the UAV.

As shown in Fig. 14, the designed bridge alignment in its complete state concerning pre-cambering is represented by the blue line. The maximum value of the abscissa in Fig. 14 is the front end of the beam, which is currently connected to the launching nose, and will fall on the top of pier 55# and be separated from the launching nose when the bridge is eventually completed (see Fig. 7). The three blue triangles in Fig. 14 respectively mark the positions of piers 53#, 54#, and 55# at the time of completion. At that point, the left side of these two spans will be connected with the other 13 spans of this continuous beam, and the right end will be simply supported. The specified longitudinal slope is not taken into account by the designed bridge alignment discussed here, hence the relative height of these three piers/supports is the same (set as 0). By adjusting the relative height of the 53# and 54# pier positions to 0, the data processed by the centroid of slice method, as well as the TS's data, are twisted to be consistent with the designed bridge alignment. The unevenness of the curve may be attributed to the steel box girder's splice and the presence of thin debris that was not fully removed during the preprocess procedure on the bridge deck. However, it is still evident that each collection of data's structural geometry exhibits the same trend and can be used for a bridge alignment inspection. The bridge in the measured section under that construction progress is supported by piers 41# and 42# (gray triangles in Fig. 14), which deviates from the support's position of the completed state of the bridge. Therefore, the current bridge alignment is affected and slightly shifts to the right. The deviation from the designed bridge alignment at pier 41# is more significant than at pier 42# because the portion of the steel box beam to the left of pier 40# is still in place on the construction platform and has not been pushed out (see Fig. 7(c)). The bridge alignment around pier 41# will recede under its effect if it is free to bend under the force of gravity. Therefore, the obtained bridge alignments agree well with the designed pre-cambering bridge alignment and the current stress state.

## 6. Conclusions

This paper proposed a practical UAV flight planning approach for oblique photography based on feature waypoints to customize the flight route for more efficient multi-view image collection. An efficient framework for automatically extracting bridge alignment from point cloud data is also introduced in this paper, and two bridge alignment extraction method is compared. With the above methods, a survey on an under-construction continuous-beam bridge is conducted using a UAV and a terrestrial laser scanner (TLS). The results show that:

- (1) The full-scale bridge's 3D model can be quickly obtained using either UAV or TLS. Due to their different operation principles,

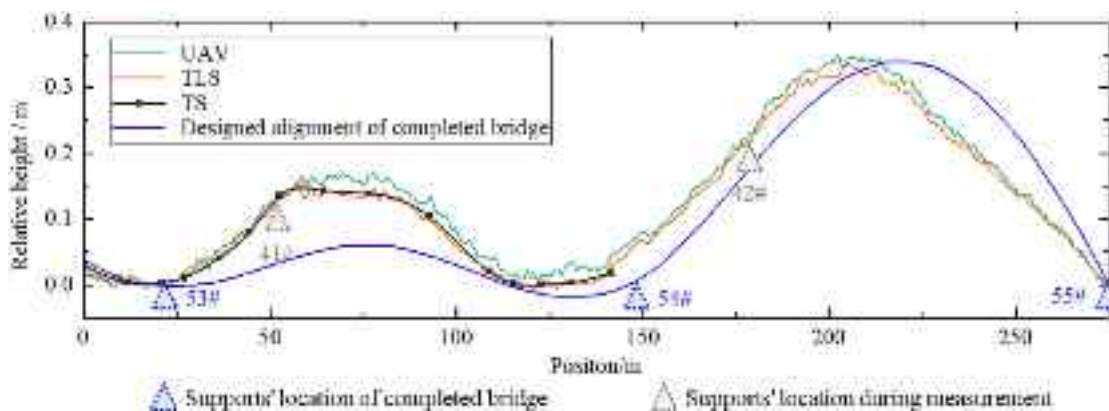


Fig. 14. Comparison with designed bridge alignment.

UAV oblique photography is more time-consuming than laser scan in data collecting and model reconstruction. However, the high maneuverability gives the UAV a distinct advantage in surveying hard-to-reach components and places.

- (2) The optimized UAV route planning method is more efficient than the frequently used strategies, circular route flight and five-way route flight, in gathering multi-view bridge images and reconstructing detailed 3D models. Optimized flight planning enhances the intricacy of every component of the reconstruction model, especially the region of supports and girder bottom, with less time and energy.
- (3) According to reference data of the total station, the centroid of slice method contributes to a lower error than the fixed-step search method of 4.41 mm and 10.97 mm at 144 m measured length using TLS and UAV, respectively, without using any GCPs and targets. The bridge alignments obtained using different devices agree well with the designed pre-cambering bridge alignment and the current stress state.

Although this study presented promising results, some limitations require further investigation. First, even though the proposed approach can determine the interpolation waypoints automatically based on the feature line/area, the feature points must still be selected manually based on experience. In addition, this paper only focused on the bridge alignment, whereas many other geometric shape parameters can be studied, such as the beam's deviation in the launching direction at different construction stages, and the piers' irregular appearance due to poor concreting quality. Furthermore, some parameters, such as overlap rate, were not elaborated upon in this study, which requires further investigation.

#### Declaration of Competing Interest

The authors declare that they have no known competing financial interests or personal relationships that could have appeared to influence the work reported in this paper.

#### Data availability

Data will be made available on request.

#### Acknowledgment

This research was funded by the National Natural Science Foundation of China (52127813), the National Key Research and Development Program of China (2020YFC1511900), the Xplorer Prize from Tencent, the Transportation Construction Science and Technology Project of Shanxi Province (2020-2-04), and the Transportation Science and Technology Project of Jiangsu Province (2021Y15).

#### References

- [1] Y. Xu, J. Zhang, UAV-based bridge geometric shape measurement using automatic bridge component detection and distributed multi-view reconstruction, *Autom. Constr.* 140 (2022), 104376, <https://doi.org/10.1016/j.autcon.2022.104376>.
- [2] J.F. Wang, J.P. Lin, R.Q. Xu, Incremental launching construction control of long multispan composite bridges, *J. Bridg. Eng.* 20 (11) (2015), [https://doi.org/10.1061/\(ASCE\)BE.1943-5592.0000737](https://doi.org/10.1061/(ASCE)BE.1943-5592.0000737), 04015006.
- [3] P.B. Tang, D. Huber, B. Akinci, R. Lipman, A. Lytle, Automatic reconstruction of as-built building information models from laser-scanned point clouds: a review of related techniques, *Autom. Constr.* 19 (7) (2010) 829–843, <https://doi.org/10.1016/j.autcon.2010.06.007>.
- [4] S. Tuttas, A. Braun, A. Borrmann, U. Stilla, Acquisition and consecutive registration of photogrammetric point clouds for construction progress monitoring using a 4D BIM, *PFG-J. Photogramm. Remote Sensing Geoinf. Sci.* 85 (1) (2017) 3–15, <https://doi.org/10.1007/s41064-016-0002-z>.
- [5] Q. Wang, M.K. Kim, Applications of 3D point cloud data in the construction industry: a fifteen-year review from 2004 to 2018, *Adv. Eng. Inform.* 39 (2019) 306–319, <https://doi.org/10.1016/j.aei.2019.02.007>.
- [6] Y.Q. Qi, N.C. Coops, L.D. Daniels, C.R. Butson, Comparing tree attributes derived from quantitative structure models based on drone and mobile laser scanning point clouds across varying canopy cover conditions, *ISPRS J. Photogramm. Remote Sens.* 192 (2022) 49–65, <https://doi.org/10.1016/j.isprsjprs.2022.07.021>.
- [7] Q. Wang, M.K. Kim, J.C.P. Cheng, H. Sohn, Automated quality assessment of precast concrete elements with geometry irregularities using terrestrial laser scanning, *Autom. Constr.* 68 (2016) 170–182, <https://doi.org/10.1016/j.autcon.2016.03.014>.
- [8] K. Yu, C.G. Zhang, M. Shooshtarian, W.J. Zhao, J.P. Shu, Automated finite element modeling and analysis of cracked reinforced concrete beams from three-dimensional point cloud, *Struct. Concr.* 22 (6) (2021) 3213–3227, <https://doi.org/10.1002/suco.202100194>.
- [9] W.J. Zhao, Y. Jiang, Y.Y. Liu, J.P. Shu, Automated recognition and measurement based on three-dimensional point clouds to connect precast concrete components, *Autom. Constr.* 133 (2022), 104000, <https://doi.org/10.1016/j.autcon.2021.104000>.
- [10] M. Puliti, G. Montaggioli, A. Sabato, Automated subsurface defects' detection using point cloud reconstruction from infrared images, *Autom. Constr.* 129 (2021), 103829, <https://doi.org/10.1016/j.autcon.2021.103829>.
- [11] F. Di Stefano, S. Chiappini, A. Gorreja, M. Balestra, R. Pierdicca, Mobile 3D scan LiDAR: a literature review, *Geomatics Nat. Hazards Risk* 12 (1) (2021) 2387–2429, <https://doi.org/10.1080/1947505.2021.1964617>.
- [12] C. Ye, S. Acikgoz, S. Pendrigh, E. Riley, M.J. DeJong, Mapping deformations and inferring movements of masonry arch bridges using point cloud data, *Eng. Struct.* 173 (2018) 530–545, <https://doi.org/10.1016/j.engstruct.2018.06.094>.
- [13] X. Zhou, J. Liu, G. Cheng, D. Li, T. Huang, J. Liang, H. Liu, Y. Liu, Intelligent virtual trial assembly of large and complex steel arch bridges based on point cloud data, *China J. Highw. Transp.* 34 (11) (2021) 1–9, <https://doi.org/10.19721/j.cnki.1001-7372.2021.11.001>.
- [14] C. Popescu, B. Taljsten, T. Blanksvad, L. Elfgren, 3D reconstruction of existing concrete bridges using optical methods, *Struct. Infrastruct. Eng.* 15 (7) (2019) 912–924, <https://doi.org/10.1080/15732479.2019.1594315>.
- [15] Y.T. Han, G. Wu, D.M. Feng, Vision-based displacement measurement using an unmanned aerial vehicle, *Struct. Control. Health Monit.* 29 (10) (2022), e3025, <https://doi.org/10.1002/stc.3025>.
- [16] F.N. He, T. Zhou, W.F. Xiong, S.M. Hasheminnasab, A. Habib, Automated aerial triangulation for UAV-based mapping, *Remote Sens.* 10 (12) (2018) 1952, <https://doi.org/10.3390/rs10121952>.
- [17] S.Y. Chen, D.F. Laefer, E. Mangina, S.M.I. Zolanvari, J. Byrne, UAV bridge inspection through evaluated 3D reconstructions, *J. Bridg. Eng.* 24 (4) (2019), [https://doi.org/10.1061/\(ASCE\)BE.1943-5592.0001343](https://doi.org/10.1061/(ASCE)BE.1943-5592.0001343), 05019001.
- [18] M. Roberts, D. Dey, A. Truong, S. Sinha, S. Shah, A. Kapoor, P. Hanrahan, N. Joshi, Submodular trajectory optimization for aerial 3D scanning, in: 2017 IEEE International Conference on Computer Vision (ICCV), Venice, Italy, 2017, pp. 5334–5343, <https://doi.org/10.1109/ICCV.2017.569>.
- [19] D. Moon, S. Chung, S. Kwon, J. Seo, J. Shin, Comparison and utilization of point cloud generated from photogrammetry and laser scanning: 3D world model for smart heavy equipment planning, *Autom. Constr.* 98 (2019) 322–331, <https://doi.org/10.1016/j.autcon.2018.07.020>.
- [20] J.P. Delgado, P.R. Soria, B.C. Arrue, A. Ollero, Bridge mapping for inspection using an UAV assisted by a total station, *Adv. Intell. Syst. Comput.* 694 (2018) 309–319, [https://doi.org/10.1007/978-3-319-70836-2\\_26](https://doi.org/10.1007/978-3-319-70836-2_26).
- [21] X. Shi, Q. Xu, H. Ma, Parametrical study and optimization using unmanned aerial vehicle measurement in bridge construction alignment, *J. Tongji Univ. Nat. Sci.* 50 (1) (2022) 32–41, <https://doi.org/10.11908/j.jsn.0253-374x.21097>.
- [22] S. Dabutarw, N.N. Kulkarni, M. Angelosanti, C. Niezrecki, A. Sabato, Sensitivity analysis of unmanned aerial vehicle-borne 3D point cloud reconstruction from infrared images, *J. Build. Eng.* 58 (2022), 105070, <https://doi.org/10.1016/j.jobe.2022.105070>.
- [23] A. Khaloo, D. Lattanzi, K. Cunningham, R. Dell'Andrea, M. Riley, Unmanned aerial vehicle inspection of the Placer River trail bridge through image-based 3D modelling, *Struct. Infrastruct. Eng.* 14 (1) (2018) 124–136, <https://doi.org/10.1080/15732479.2017.1330891>.